Renewable Energy 250 (2025) 123231

Contents lists available at ScienceDirect

Renewable Energy

journal homepage: www.elsevier.com/locate/renene

Supercritical CO_2 hybrid Brayton–Organic Rankine Cycle integrated with a solar central tower particle receiver: Performance, exergy analysis, and choice of the organic refrigerant

J.A. Moctezuma-Hernandez *, R.P. Merchán, J.M.M. Roco

Department of Applied Physics and IUFFYM, Universidad de Salamanca, Spain

ARTICLE INFO

Keywords:
Supercritical CO_2 (sCO_2)
Hybrid Brayton–Organic Rankine Cycle (ORC)
Solar central tower
Silicon carbide (SiC) particle receiver
Exergy analysis
Heat transfer fluid (HTF)

ABSTRACT

A study of the integration of a supercritical CO_2 hybrid Brayton–Organic Rankine Cycle (ORC) with a Concentrated Solar Power (CSP) system using a particle receiver is presented. It focuses on evaluating the energy and exergy performance of the system to improve its efficiency and reduce fuel consumption. The particle receiver uses a mixture of silicon carbide and air as the working fluid, allowing operation at higher temperatures suitable for coupling with the supercritical CO_2 Brayton cycle. Detailed thermodynamic models were developed using Mathematica and Engineering Equation Solver (EES) to simulate the behavior of the system under various conditions. The results show that coupling the particle receiver with the hybrid Brayton cycle significantly reduces fuel consumption by 63.2%. The exergy analysis shows that the highest exergy destruction occurs in the heat exchangers of the entire system, indicating potential areas for further efficiency improvements. The study also highlights the critical role in system performance of the ORC working fluid used in the bottoming cycle. Among the fluids tested, R600a was found to be the most effective, providing the highest efficiency under the considered conditions. The results highlight the potential of integrating particle receivers into CSP systems to improve both the energy efficiency and sustainability of power generation, and thus, it represents a promising approach for achieving more effective and sustainable power generation.

1. Introduction

Anthropogenic climate change is a current problem that affects the society. The "Intergovernmental Panel on Climate Change (IPCC) 2022 report: Impacts, Adaptation and Vulnerability" [1] states that human-induced climate change has caused environmental and human problems around the world. This report emphasizes the importance of limiting global warming to 1.5 °C to achieve a more just, equitable and sustainable world. Renewable energy has an important role to play in achieving this goal. Nowadays, this type of energy accounts for 14% of global demand [2], while 80% of electricity demand is met by burning natural gas and petroleum products [3].

In this respect, solar energy is a viable alternative, and it is expected that by 2050, this type of energy will account for the largest energy demand among the different energy sources including non renewable energies [4]. Solar thermal energy has a great potential to compete with and replace conventional energy systems. This energy is used in applications such as heat pumps, electric power generation, and industrial processes like pasteurization, distillation, and boiler water heating [5]. Concentrated Solar Power (CSP) has many advantages over other solar collection techniques. The most important advantages are flexibility, reliability and the possibility of integrating Thermal Energy Storage (TES), which allows for continuous production even in the absence of solar energy [6]. The Heat Transfer Fluid (HTF) operating inside the particle receiver, which must operate at high temperatures, is an important aspect for this kind of systems. Both Fluidized beds or Dense Particle Suspensions (DPS) can be used as HTF. DPS consist of very small particles that can be fluidized at a low gas velocity (5.5 mm/s). They can reach temperatures above 500 °C [7] and achieve a convection coefficient between the solar collector and the HTF of 500 W/m^2-K [8]. A fluidized bed is a system in which solid particles are suspended in an upward flow of gas, creating a dynamic mixture that exhibits fluid-like behavior. This phenomenon significantly enhances heat transfer due to increased particle–gas interactions, making it a highly effective medium for thermal energy applications. In the CSP systems, fluidized beds, particularly DPS, offer a promising alternative as heat transfer and storage media. This makes the DPS a great alternative as a HTF within the particle receiver. This thermal energy can then be used to produce electrical energy by coupling it to a power cycle,

* Corresponding author.
E-mail address: ja.moctezuma@usal.es (J.A. Moctezuma-Hernandez).

https://doi.org/10.1016/j.renene.2025.123231
Received 13 November 2024; Received in revised form 8 April 2025; Accepted 21 April 2025
Available online 3 May 2025

Nomenclature

Abbreviations Symbols

DPS	Dense particle suspension
HTF	Heat transfer fluid
HTR	High temperature recuperator
LTR	Low temperature recuperator
ORC	Organic Rankine cycle
$SCBC$	Supercritical Brayton cycle

Greek symbols

α	Convective heat transfer coefficient (W/m^2-K)
η	Thermal efficiency (–)
μ	Viscosity (kg/m-s)
ρ	Density (kg/m^3)
φ	Volumetric fraction (–)

Symbols

$\dot{E}$	Exergy flow rate (MW)
$\dot{m}$	Mass flow (kg/s)
$\dot{Q}$	Heat transfer rate (MW)
$\dot{W}$	Power (MW)
Cp	Specific heat (J/kg-K)
G	Mass flow per unit area (kg/m^2-s)
k	Thermal conductivity (W/m-K)
P	Pressure (bar)
P_r	Prandtl number (–)
R_e	Reynolds number (–)
T	Temperature (K)

Subscripts

a	Ambient
$base$	Base
cv	Control volume
e	Exit
f	Fluidized bed
g	Gas
GT	Gas turbine
i	Input
p	Particle
t	Tube
VT	Vapor turbine

such as a supercritical CO_2 (sCO_2) cycle. An important advantage of using this cycle is that it reduces the cost of electricity due to its high efficiency [9–11].

In recent years, several works have been carried out to analyze the behavior of fluidized beds as HTF inside of the particle receiver. For example, Jiang et al. [12] conducted an analysis of the thermal and heat transfer performance in a particle solar receiver. They used finite element techniques to study the radiation flux distribution in the particles, and observed that particles with diameters between 0.2 and 0.4 mm offered better output temperatures and thermal conversion efficiencies. They also showed that particles closer to the sunlight entrance window absorb more direct radiation, while the absorption of particles further away depends on the radiant energy of nearby particles. The particles used in the receiver also play an important role. Perez Lopez et al. [13] studied the use of DPS as a heat transfer fluid in a solar receiver, using silicon carbide (SiC) because its thermodynamic properties are suitable for this type of application and it is easy to fluidize. SiC DPS has advantages over other HTFs, such as molten salts, mineral oils, or water, which present a limited temperature range, high pressure, low energy storage capacity, and are corrosive and toxic. Perez Lopez et al. [13] used a 150-kW receiver consisting of 16 tubes, which allows the particles to circulate continuously in a closed loop. Using this inputs the particle temperature reached 700 °C at the outlet of the tubes and the receiver efficiency ranged from 50% to 90%. Boissiere et al. [14] conducted an experiment using DPS as a heat transfer fluid for CSP applications. They used SiC as particles because of its high working temperature, good thermal conductivity and low cost. Some important input values of this work are: the particle size is 60 μm, the mass flow rate of DPS in the receiver varies from 20 kg/h to 130 kg/h, the tubes used have a height of 2.16 m and an internal diameter of 32 mm. They showed that this type of DPS offers a heat storage capacity similar to that of thermal fluids, without the need of high pressurization, and allowing high operation temperatures. For these findings, it is observed that it is essential to control the distribution of the particles along the entire length of the tube to ensure the stability and efficiency of the system. The most important parameters to achieve this stability are the solid feed rate, the fluidization velocity and the pressure.

The conversion of thermal to electrical energy is also performed coupling the power systems with these CSP systems. Brayton cycles with supercritical carbon dioxide as the working fluid have been used with this purpose, as they present an energy efficiency close to 50% [15]. Other advantages of using CO_2 as working fluid are the low temperature of its critical point, 31.1 °C, and the fact that sCO_2 is abundant, cheap, non-explosive and non-combustible [16,17]. Besides, the density of the working fluid is higher throughout the power cycle, resulting in small turbomachinery components [18,19]. The use of compact power elements can add value by reducing overall costs. In this regard, Khatoon and Kim [20] conducted an analysis of a Brayton cycle with sCO_2 as the working fluid coupled to a central tower receiver. They obtained and overall efficiency of 45% considering recompression and regenerative settings and determining the best climatic location for this setting. Likewise, exergy analysis is of great help in this type of energy systems, since it allows to evaluate the efficiency and the cost per unit of energy in order to minimize the operation and maintenance costs, and to improve the design and operation of the system. In this sense, Organic Rankine Cycles (ORC) are a promising solution to take advantage of the high thermal potential of the fluid exiting the turbine, converting low-temperature waste heat into electrical energy [21–24]. Unlike conventional Rankine cycles, ORC systems do not use water, but rather organic fluids which present more suitable thermodynamic properties allowing operation at lower temperatures, improving the overall efficiency by harnessing energy that otherwise would be lost [25]. Akbari and Mahmoudi [26] performed a thermo-economic analysis and optimization of a recompression Brayton cycle with sCO_2 coupled to an ORC. They analyzed eight different working fluids in the ORC, including isobutane and RC318, with good exergy efficiency. They conclude that the RC318 has the best unit production cost in the ORC. Comparing the Brayton cycle alone to its coupling with the ORC shows an increase in exergy efficiency by 11.7% when the ORC setup is used, highlighting the advantages of the coupled configuration. On the other hand, Tang et al. [27] performed a thermo-economic analysis and optimization of different organic flash cycles with a recompression Brayton cycle (RBC) using sCO_2. Different configurations in the ORC were analyzed, such as basic organic flash cycle (BOFC), regenerative organic flash cycle (ROFC), and organic flash cycle (OFRC). The results showed that the thermal efficiency and the exergy efficiency rise linearly with the increase of the turbine 1 inlet temperature from 550 °C to 650 °C. The sCO_2 RBC/OFRC system showed the highest thermal and exergy efficiencies as well as the lowest total capital cost compared to the other systems. Different working fluids were evaluated, and it was found that R1336mzz(Z) provided the highest exergy efficiency for the

sCO_2 RBC/BOFC and sCO_2 RBC/ROFC systems, while R1224yd(Z) was the most efficient for the sCO_2 RBC/OFRC system. Finally, a multi-objective optimization was performed to maximize exergy efficiency and minimize total capital cost, highlighting the necessity to balance thermodynamic and economic performance in system design.

In this work all these results detailed above are considered by proposing a model combining the three above mentioned systems: solar dense particle receiver, sCO_2 hybrid Brayton Cycle and bottoming Organic Ranking Cycle as a promising scheme. For this purpose, a central tower particle receiver with a fluidized bed (air mixture with SiC) as working fluid is modeled. Heat transfer process between the solar radiation from the heliostat field and the HTF inside the receiver is simulated setting the temperature at the receiver outlet to 650 °C in order to calculate the number of tubes needed to reach it. This also requires to model the heat transfer process inside the receiver. The energy at the receiver outlet is exploited by coupling a Brayton sCO_2 cycle to generate electrical power. A parametric analysis between the receiver coupling and the power cycle has been performed to determine the value of the parameters that mostly affect the fuel consumption of the Brayton cycle. An ORC system is coupled to the gas turbine exhaust to harness the thermal power of the gas turbine gases. R600, R600a, R1234yf, R1234ze(E), R134a, R152a, R114, R245fa, and Isopentane are analyzed for the ORC system in order to choose the one with the best energy and exergy performance and environmental friendliness. For these purpose an exergy analysis is performed on the entire system to identify the components that require improvement to enhance both individual and overall performance. The novelty of this work lies in the integration and modeling of three energy systems: a particle receiver, a Brayton sCO_2 cycle, and an organic Rankine cycle (ORC). The overall system efficiency is analyzed, demonstrating a 63.2% reduction in fuel consumption. Additionally, various refrigerants are assessed for the ORC, considering their energy efficiency, exergetic performance, and environmental viability. The results leads to consider that R600a is the most suitable option. Moreover, it is observed that this refrigerant contributes to 36.9% of the total power produced. An exergetic analysis is also conducted to identify the components with the highest exergy destruction, revealing that heat exchangers exhibit the greatest losses, highlighting an opportunity for optimization. A parametric analysis is performed on the particle receiver, in order to study the influence of variables such as volumetric fraction, gas velocity, tube diameter, and heliostat field power. The findings show that the tube diameter and volumetric fraction have the most significant impact on receiver efficiency.

2. System description and modeling

The model of the particle receiver system and the heat transfer between the heliostat field radiation and the fluidized bed presented in this work is based on the works performed by Gallo et al. [28] and Córcoles et al. [29]. The modeling of the sCO_2 hybrid Brayton cycle and ORC performance requires evaluating the mass, energy and exergy balances for each component [30]. For this modeling Mathematica [31] and Engineering Equation Solver (EES) [32] have been used, and all the equation introduced in Sections 2.2, 2.3 and 2.4 will be computed using these two software programs.

2.1. System description

Fig. 1(a) describes the layout used for the conversion of the solar energy collected by the solar tower into mechanical energy. This conversion is carried out by three subsystems: the Particle Receiver, the Hybrid Brayton Power System, and the Organic Rankine Cycle (ORC). The Particle Receiver system consists of the solar tower collection chamber and a setup producing the fluidized bed particles, as shown in Fig. 1(b). Solar radiation strikes a tube containing silicon particles mixed with air, which are supplied by a compressor. The compressor ensures the fluidization of the silicon particles contained in the hopper and facilitates the upward movement of the particles. A feed screw continuously supplies particles to the absorption tube, where the heliostat field directs solar radiation, which is absorbed as heat by the fluidized bed. At the solar receiver's outlet, the fluidized bed is connected to a heat exchanger (HEX 1), where the thermal energy of the fluidized bed is transferred to the power system composed of a combined cycle: an upstream supercritical CO_2 (sCO_2) Hybrid Brayton Cycle (SCBC) and a bottoming Organic Rankine Cycle (ORC). The SCBC and ORC are connected in turn by HEX 2, where the surplus thermal energy of the SCBC is absorbed by the ORC. Finally, Fig. 1(c) presents the T-s diagram of the sCO_2 Brayton cycle, highlighting key energy contributions: solar energy input between states x and z, heat addition from the combustion chamber between states z and 3, and the ORC cycle energy integration between states yx and 1.

The system proposed is inspired in Reyes-Belmonte et al. work [33] but considering the advantages of sCO_2 as working fluid, pointed above and introducing the possibility of a continuous power production by hybridizing with a combustion natural gas chamber. Indeed, a bottoming ORC is proposed to harness the thermal power of the sCO_2 for producing electrical energy

2.2. Particle receiver

The model of the particle receiver system and the heat transfer between the heliostat field radiation and the fluidized bed presented in this work is based on the works performed by Gallo et al. [28] and Corcoles et al. [29].

Gallo et al. equations describing the particle receiver have been validated in the context of dense particle suspension solar receivers and have proven effective in characterizing heat transfer and fluid dynamics in central tower systems using SiC particles. Specifically, the model developed by Gallo et al. provides a reliable estimation of thermodynamic properties, particle and gas mass flow, and geometric parameters, all of which are essential for evaluating the receiver's thermal efficiency. Additionally, these equations have been utilized in the design of both pilot-scale and large-scale receivers, reinforcing their relevance to this study. The assumptions made on the particle receiver model are:

- The sliding velocity between gas and particles in dense suspensions is approximately equal to the minimum flow velocity, regardless of flow conditions.
- The density, heat capacity and thermal conductivity of the dense suspension are considered as function of the volumetric fraction of particles. This approach is based on previous models [34].
- Radiative heat transfer is included as a function of the emissivity of the particles and the tubes walls, as well as the average temperature of the system.
- The convective coefficient is approximately 70% of the maximum coefficient.
- The particle flow coming upwards is considered to improve the control of the system and adjust the residence time inside the receiver.

The fluidized bed circulating inside the particle receiver is a mixture of silicon carbide and air whose thermodynamic properties are calculated as follows. Table 1 shows the values of the properties of silicon carbide. All thermodynamic properties were evaluated using the mean temperature $\left(T_{mean} = \frac{T_p^{in}+T_p^{out}}{2}\right)$, where T_p^{in} and T_p^{out} are the inlet and outlet temperature of particles of the fluidized bed of the receiver, respectively. From Eqs. (1)–(6) [28], the mass flow per unit area of the fluidized bed, G_{DPS}, the density, ρ_{DPS}, and the specific heat of the fluidized bed, $C_{p,DPS}$, are calculated using the input data from Tables 1 and 2. The thermodynamic properties of the gas (ρ_g, $C_{p,g}$, k_g, μ_g), required in the calculation performed below are obtained using the

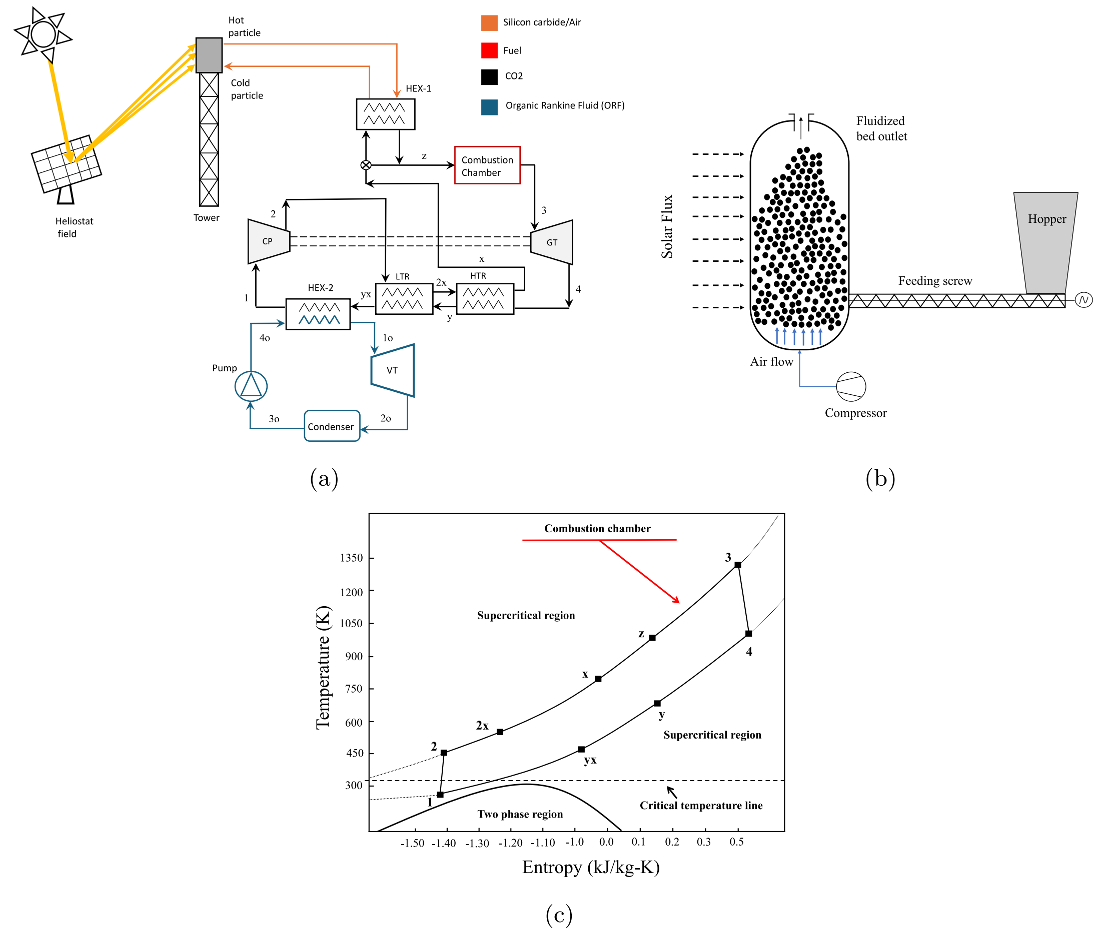

Fig. 1. (a) Schematic of particle receiver coupled to Supercritical Brayton Cycle/Organic Rankine Cycle (SCBC/ORC). (b) Scheme of the system which provide the fluidized bed system to the particle receiver. (c) T-s diagram of supercritical CO_2 Brayton cycle.

REFPROP database [35]. For the modeling of the particle receiver a fluidized bed outlet temperature $T_p^{out} = 923$ K is fixed, and the receiver inlet temperature $T_p^{in} = 423$ K is obtained through an iterative process. Initially, an assumed temperature was considered. The iteration process is adjusted based on the energy balance and heat transfer equations until convergence was reached. The value of T_p^{in} ensures the correct evaluation of the thermodynamic properties of both the gas and the silicon carbide for every iteration, as they are assessed at the mean temperature, T_{mean}. The iterative methodology is detailed in Fig. 2. The convergence criterion chosen compares the thermodynamic properties of the last iteration with the current one, and when the difference is less than a fixed level of precision, for instance 0.01 K in temperature, the iterative process ends.

$$G_{DPS} = \varphi_p \rho_p (u_g - u_{mf}) + (1 - \varphi_p)\rho_g u_g \tag{1}$$

$$\rho_{DPS} = \varphi_p \rho_p + (1 - \varphi_p)\rho_g \tag{2}$$

$$C_{p,DPS} = \frac{\varphi_p \rho_p C_{p,p} + (1 - \varphi_p)\rho_g C_{p,g}}{\varphi_p \rho_p + (1 - \varphi_p)\rho_g} \tag{3}$$

$$k_{DPS} = k_g \left[1 + \frac{3\varphi_p (f_\lambda - 1)}{1 + f_\lambda - \varphi_p (f_\lambda - 1)}\right] \tag{4}$$

$$f_\lambda = \frac{k_p}{k_g} \tag{5}$$

$$\mu_{DPS} = \mu_g \left[f_p \left(\frac{1 - \varphi_p}{f_p - \varphi_p}\right)\right]^{\frac{2.5 f_p}{1 - f_p}} \tag{6}$$

These equations are expressed in terms of the volumetric fraction of particle suspension, φ_p; the gas velocity, u_g; the minimum fluidization velocity, u_{mf}; and the specific heat of the particle and gas, $C_{p,p}$, $C_{p,g}$, respectively. The others values of Eq. (1)–(6) are defined in Tables 1 and 2. Once the thermodynamic properties are known, the fluidized bed mass flow, which is the sum of the gas and particle mass flow, is calculated from Eqs. (7)–(9) [28]. It requires to carry out an energy balance inside the particle receiver, Eq. (7), and then to calculate the particle mass flow and the gas mass flow from Eqs. (7) and (8), respectively. Finally the mass flow rate of the fluidized bed, $\dot{m}_{DPS}$ is calculated from Eq. (9). The data in the Tables 1 and 2 are used to evaluate the Eqs. (1)–(9).

$$\dot{m}_p = \frac{\dot{Q}_{rec}}{C_{p,p}(T_p^{out} - T_p^{in})} \tag{7}$$

$$\dot{m}_g = \frac{(1 - \varphi_p)\rho_g u_g}{\varphi_p \rho_p (u_g - u_{mf})} \dot{m}_p \tag{8}$$

$$\dot{m}_{DPS} = \dot{m}_g + \dot{m}_p \tag{9}$$

In Eq. (7), $C_{p,p}$ is the heat capacity of the particle and is provided by using data from NIST [36] as follows: $C_{p,p} = AT_{mean}^3 + BT_{mean}^2 + CT_{mean} + D$, where $A = 2 * 10^{-9}$, $B = -2 * 10^{-5}$, $C = 0.0408$, $D = 19.685$ (J/Kg K).

Then, the number of tubes necessary to achieve the fixed outlet temperature, $T_p^{out} = 923$ K, is calculated from Eqs. (10), (11), and the mass flow rates previously calculated. In addition, the heat transfer analysis described below in this section must be performed.

$$N_{tubes} = \frac{4\dot{m}_{DPS}}{\pi d_i^2 G_{DPS}} \tag{10}$$

$$A_{tubes} = N_{tubes} \pi d_i T H \tag{11}$$

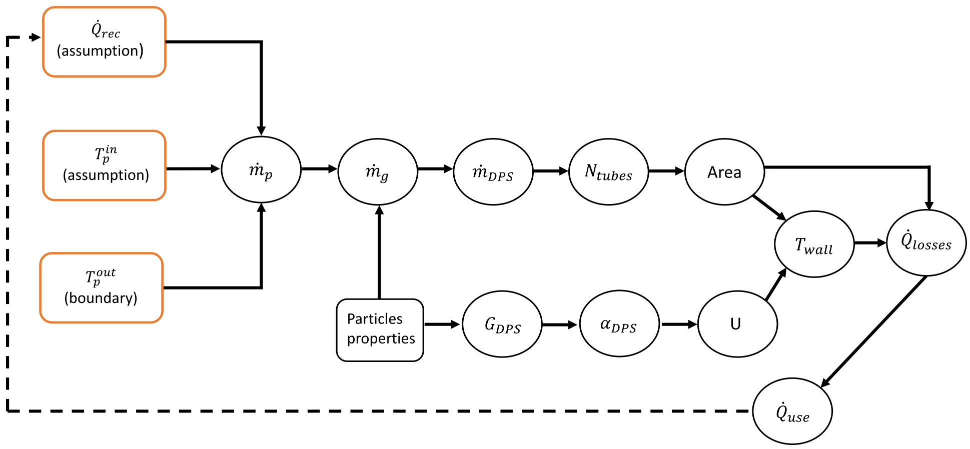

Fig. 2. Iterative process for particle receiver modeling [33].

Table 1
Silicon carbide particles properties [33].

Property	Units	Value
Sauter mean diameter (d_p)	(μm)	63.9
Density (ρ_p)	(kg m−3)	3210
Thermal conductivity (k_p) (at 500 °C)	(W m−1 K−1)	109
Sphericity (ϕ_s)	–	0.77

Table 2
Input data for the particle receiver simulation [28,33].

Parameters	Units	Value
Input power from heliostat field ($\dot{Q}_{rec}$)	(MW)	57[a]
Mean Flux (Q_{flux})	(kW/m^2)	400[a]
Fluidized bed outlet temperature (T_{fout})	(K)	923
Volumetric fraction of particle (φ_p)	–	0.6
Minimum fluidization velocity (u_{mf})	(mm/s)	5.5
Gas velocity (u_g)	(mm/s)	125
Density factor (f_p)	–	0.64
Ambient temperature (T_a)	(K)	298
Inner tube diameter (d_i)	(mm)	41[a]
Tubes height (TH)	(m)	8.0[a]
Active frontal fraction (f_{act})	–	0.33

[a] Value taken from Ref. [33].

In Eq. (10)d_i is the internal diameter of the tube, and in Eqs. (10)–(11), N_{tubes} and A_{tubes} represent the number of tubes and the total area of the tubes needed in the receiver, respectively.

The next step in the analysis involves performing the heat transfer calculations inside the particle receiver, as illustrated in Fig. 2. Developing a model to describe the heat transfer process within the particle receiver is complex. The energy transfer process starts when solar radiation from the heliostat field incident on the tubes. This radiation heats the tube wall and increases its temperature, which in turn allows the fluidized bed to be heated by convection and conduction, causing the particles to gain a higher temperature. This energy transfer process is schematically described in Fig. 3. Where, t_t is the thickness of the tube and k_t is the thermal conductivity of the tube, the values are described below.

To start with the computation of heat transfer, it is necessary to know the value of the convective coefficient of the fluidized bed, α_{DPS}. This coefficient has special interest because it is responsible for modeling the energy transfer inside the particle receiver. The correlations used come from the work developed by Molerus and Wirth [37] and used by Gallo et al. [28]. The way to perform this analysis can be empirical or semi-empirical, in this work as it will be pointed below semi-empirical correlations were used. Eq. (12) allows for the computation of the heat transfer coefficient, involving the convective coefficient, α_{DPS}, which as it is assumed only contributes 70% to the total heat transfer coefficient [37]. On the other hand, the radiative heat transfer between the particles and the tube is evaluated from Eq. (13), where ε_p, ε_t are the emissivity of the particle and tube, respectively. σ is the Stefan–Boltzmann constant.

$$\alpha_{DPS} = 0.7\alpha_w + \alpha_{rad} \tag{12}$$

$$\alpha_{rad} = 7.3(\varepsilon_p \varepsilon_t \sigma T_{mean}^3) \tag{13}$$

Evaluating α_{DPS} from Eq. (12) requires a prior evaluation of α_w, which can be performed by using the semi-empirical correlations, Eqs. (14)–(17), proposed in the work of Córcoles et al. [29]. The selection of the correlations proposed by Córcoles et al. is based on their proven performance in fluidized bed systems within vertical tubes, using SiC as the granular material and particles with a diameter of 64 μm. In these studies, the tube had a diameter of 40 mm and a wall temperature of 700 ° C. Since these conditions are replicated in the present work, the selected correlations are expected to provide an accurate prediction of the system's behavior. In Eqs. (14)–(15), α_g is the contribution of the gas heat transfer and α_p the one of the particles heat transfer, f_p is the coefficient of the particle volume fraction at the wall, which depends on the particle volumetric fraction, φ_p, and the cell volume fraction, φ_{cp}. Finally, α_{gp} refers to the heat transfer contribution between gas and particle interaction.

$$\alpha_w = \alpha_g + f_p \alpha_p + \alpha_{gp} \tag{14}$$

$$f_p = 1 - e^{-10\left(\frac{\varphi_p}{\varphi_{cp}}\right)} \tag{15}$$

$$\alpha_g = \left(c_0 Re_L^{n_1} Pr^{n_2} + c_1\right) \frac{k_g}{L} + c_2 \tag{16}$$

$$\alpha_p = \left(c_3 Re_p^{n_3}\right) \frac{k_g}{d_p} \tag{17}$$

$$Pr = \frac{(\mu_{DPS})(Cp_{DPS})}{k_{DPS}} \tag{18}$$

$$Re_p = \frac{\rho_p u_g d_p}{\mu_g} \tag{19}$$

$$Re_L = \frac{\rho_g u_g TH}{\mu_g} \tag{20}$$

In Eqs. (16)–(17), Re_L is the Reynolds number, P_r is Prandtl number, k_g is thermal conductivity of the gas and d_p is particle diameter. c_0, c_1, c_2, c_3 are coefficients that have values of 0.46, 3.66, 0, 0.525 $\frac{W}{m^2K}$, respectively. Also n_1, n_2 and n_3 are coefficients whose values are 0.5, 0.33 and 0.75, respectively [38,39].

The heat transfer between the fluid phase and the particle phase is modeled with the fluid–particle heat transfer coefficient, α_{gp}, from

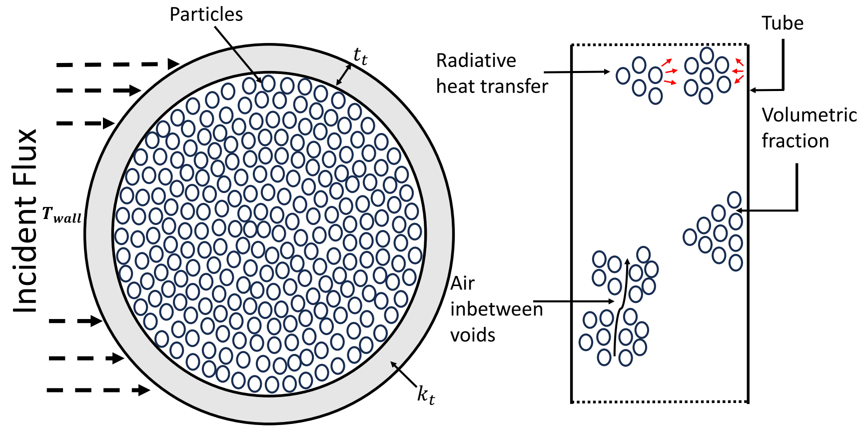

Fig. 3. Heat transfer process inside the receiver.

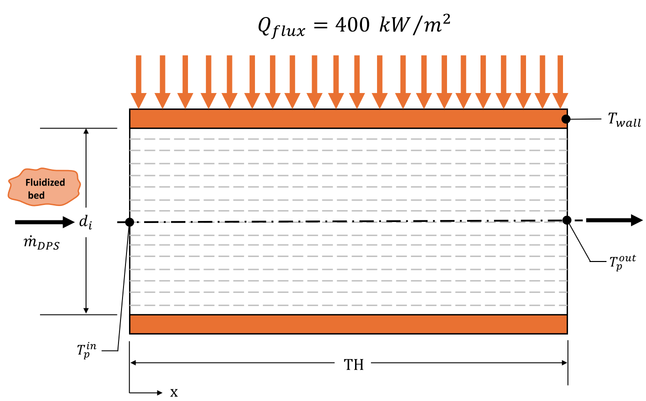

Fig. 4. Calculation of pipe wall temperature.

Eq. (21). Where, c_4, c_5, c_6, n_4 and n_5 are coefficients that have values of 0.37, 0.1, 0 $\frac{W}{m^2 K}$ and 0.6, 0.33, respectively. These values are chosen according to Ref. [40].

$$\alpha_{gp} = \left(c_4 Re_p{}^{n_4} P_r^{n_5} + c_5\right) \frac{k_g}{d_p} + c_6 \tag{21}$$

The entire energy transfer process is described using the global heat transfer coefficient (U), which is obtained from Eq. (22) [41]. This coefficient is derived from the analysis of the global heat transfer coefficient in cylindrical coordinates. All the variables in this equation have already been calculated or obtained previously in the paper.

$$U = f_{act}\alpha_{DPS} + 2\frac{\sqrt{\alpha_{DPS} k_t t_t}}{\pi d_i} \tanh\left[\pi\left(d_i + \frac{t_t}{2}\right)\left(\frac{1-f_{act}}{2}\right)\sqrt{\frac{\alpha_{DPS}}{k_t t_t}}\right] \tag{22}$$

Where f_{act} is the active front fraction of the tube, which only considers the part where the solar radiation is striking the tube, as shown in Fig. 4, and whose value is given in Table 2. The thermal conductivity and thickness of the tube are considered as $k_t = 14.2$ W/mK [42] and $t_t = 3.2$ mm [7], respectively, which correspond to an AISI 310S stainless steel tube.

Once the heat transfer process is described, the temperature at the wall of the tube, T_{wall}, can be calculated, assuming that the tube has a constant heat flow and using Newton's law of cooling equation [41], in which the heat flow is considered to not impact the entire circumference of the tube. This process is described in Fig. 4 and T_{wall} is calculated from Eq. (23). Care must be taken to avoid reaching the melting temperature of the material, which is 1127–1187 K for AISI 310S stainless steel [42]. Based on the temperature of the tube wall, the heat losses, $\dot{Q}_{losses}$, can be determined using Eq. (24) once $\dot{Q}_{conv}$ and $\dot{Q}_{rad}$ are calculated from Eqs. (25) and (26), respectively. Finally, using Eq. (27), the process is fed back with the obtained value of $\dot{Q}_{use}$, allowing the iterative cycle shown in Fig. 2 to be completed once the inlet temperature of the particles is recalculated using Eq. (7).

$$Q_{flux} = f_{act}\alpha_{DPS}(T_{wall} - T_{mean}) \tag{23}$$

$$\dot{Q}_{losses} = \dot{Q}_{conv} + \dot{Q}_{rad} \tag{24}$$

$$\dot{Q}_{conv} = (1 - f_{act})\alpha_{DPS} A_{tubes}(T_{wall} - T_a) \tag{25}$$

$$\dot{Q}_{rad} = (1 - f_{act})\epsilon_t \sigma A_{tubes}(T_{wall}^4 - T_a^4) \tag{26}$$

$$\dot{Q}_{use} = \dot{Q}_{rec} - \dot{Q}_{losses} \tag{27}$$

2.2.1. Performance criteria

The thermal efficiency of the particle receiver, η_{threc}, is used to evaluate the performance of the system. It is defined from Eq. (28) as the actual heat absorbed by the fluidized bed divided by the ideal heat that could be absorbed. The evaluation of the actual heat depends on convective and radiative heat losses, see Eqs. (24) and (27), as well as on the power supplied to the compressor and the mechanism to move the particles. Finally, the energy consumed by the compressor to move the air, $\dot{E}_{comp}$, and the energy required by the mechanism to transport the particles to the receiver, $\dot{E}_{screw}$, are obtained from Eqs. (30) and (31), where η_{mec} and η_p represent the mechanical and polytropic efficiencies, respectively. For this analysis, η_{mec}=0.8 and η_p=0.98 [43]. In Eq. (32) [28] the necessary pressure in the fluidized bed is calculated for the system to work properly. The value of parameters required in Eqs. (30)–(32) are obtained from Eqs. (1)–(6), and from the Table 2.

$$\eta_{threc} = \frac{\dot{Q}_{total}}{\dot{Q}_{rec}} \tag{28}$$

$$\dot{Q}_{total} = \dot{Q}_{use} - \dot{E}_{screw} - \dot{E}_{comp} \tag{29}$$

$$\dot{E}_{screw} = \frac{\dot{m}_p(P_{base} - P_a)}{\eta_{mec} f_p \rho_p} \tag{30}$$

$$\dot{E}_{comp} = \frac{\dot{m}_g C_{p,g} T_a}{\eta_{mec}}\left[\left(\frac{P_{base}}{P_a}\right)^{\frac{r_g}{\eta_p C_{p,g}}} - 1\right] \tag{31}$$

$$P_{base} = P_a + g\rho_{DPS} TH + 0.184\left(\frac{G_{DPS} d_i}{\mu_{DPS}}\right)^{-0.2} \frac{TH}{d_i} \frac{G_{DPS}^2}{2\rho_{DPS}} \tag{32}$$

2.3. Power block

The previous description of the heat transfer process inside the solar collector allows for the determination of the fluidized bed outlet temperature. Subsequently, the supercritical CO_2 Brayton cycle, which converts the heat absorbed by the fluidized bed into power, must be described and modeled. Fig. 1(a) shows the schematic of the cycle under analysis, where each color represents the working fluid used in different parts of the power block. The temperature versus specific entropy (T-s) diagram of the sCO_2 Brayton cycle is shown in Fig. 1(c).

The system configuration includes a high-temperature recuperator (HTR) that harnesses the turbine exhaust heat to preheat the gas exiting the compressor. This scheme was previously proposed by Santos et al. [44], whose input data for the Brayton cycle were also adopted, as the mass flow and efficiency of heat exchangers. The configuration incorporating a low-temperature heat recovery (LTR), which regulates the sCO_2 temperature to optimize the performance of the bottoming organic cycle, is based on the work of Akbari and Mahmoudi [26]. Furthermore, the sCO_2 working fluid flow in the Brayton cycle is assumed to match that of the SOLUGAS facility [45] to validate the thermodynamic model.

As shown in Fig. 1(a), the sCO_2 enters the compressor with a temperature T_1, then it is compressed until it reaches a pressure P_2 and a temperature T_2. Then, sCO_2 flow coming out of the compressor enters the recuperator of low temperature (LTR) and exchanges heat with the flow coming out of the high temperature recuperator (HTR). These components enable the recovery of a portion of the turbine's exhaust heat to preheat the working fluid before it enters the combustion chamber. This process enhances the system's thermal efficiency and reduces fuel consumption. The temperature T_{2x} is determined through an energy balance inside the LTR, using the input data from Table 3. Subsequently, to continue with the cycle, another energy balance is performed inside the HTR to obtain the temperature T_x. Next, a new heat input from the solar receiver is added. This occurs in the heat exchanger number one (HEX-1), where the fluidized bed of the solar receiver enters the exchanger and transfers energy in the form of heat to the sCO_2, which exits at a temperature T_z. Then, an energy supply from a combustion of a natural gas chamber is absorbed in HEX-2 in order to achieve the desired working temperature, T_3, of the gas turbine. In the gas turbine an expansion takes place to produce work. Finally, within heat exchanger two (HEX-2), once the sCO_2 flux has exchanged heat in HTR and LTR, the waste heat coming from the Brayton cycle is used to produce electrical energy by means of an organic Rankine cycle.

The organic Rankine cycle has, besides the HEX-2, a turbine, a condenser and a pump. In this work an analysis of different refrigerants with low Global Warming Potential (GWP) and low toxicity and flammability [46] will be performed to identify the one with the best behavior. In the model of the power system presented below the following statements are assumed:

- The pressure drop in the tubes and heat exchangers is negligible.
- The system reaches steady state.
- The expansion and compression processes are carried out adiabatically.
- All components are well insulated.

2.3.1. Power cycle model (Brayton cycle)

The Brayton sCO_2 cycle is an efficient alternative for converting thermal energy into electrical energy thanks to its high thermal efficiency and compact component size compared to conventional power cycles. This cycle operates with CO_2 in a supercritical state, meaning the substance remains above its critical point (31.1 °C, 73.8 bar). In this supercritical state, CO_2 exhibits properties of both a gas and a liquid, leaving aside the thermodynamic state 1, as illustrated in Fig. 1(c).

In this study, a regenerative Brayton cycle configuration is employed, incorporating HTR and LTR heat exchangers. By performing a mass and energy balance in each component, it is possible to determine the temperatures, heat and work of the streams involved in the cycle, see Eqs. (33) and (34). The energy balance in the heat exchangers (HTR, LTR, HEX-1 and HEX-2) considers the efficiency of each device. The input data for the SCBC are shown in Table 3.

Table 3
Input data for SCBC and ORC simulation [26,44,45,47].

Subsystem	Parameters	Value
Supercritical CO_2 Brayton Cycle (SCBC)	T_1 (K)	298
	P_1 (bar)	74.6
	r_p	4.5
	T_3 (K)	1322
	$\dot{m}$ (kg/s)	17.9
	ϵ_{HC}	0.98
	ϵ_{HS}	0.78
	ϵ_n	0.775
	$\dot{Q}_{LHV}$ (MW)	47.141
	η_c	0.98
	η_{CP}	0.815
	η_{GT}	0.885
Bottoming cycle (ORC)	T_{1_o} (K)	360
	P_{1_o} (bar)	5.37
	P_{2_o} (bar)	1.02
	$\dot{m}_o$(kg/s)	39
	η_{pump}	0.9
	η_{VT}	0.91

$$\sum \dot{m}_{in} = \sum \dot{m}_{out} \tag{33}$$

$$\sum \dot{Q} + \sum \dot{m}_{in} h_{in} = \sum \dot{W} + \sum \dot{m}_{out} h_{out} \tag{34}$$

For the design and performance evaluation of the HEX-1, an energy balance is conducted between the fluidized bed and sCO_2 side. Eq. (35) describes the heat transfer process within this system, where $T_{\text{Hotparticles}}$ represents the temperature of the particulate material at the outlet of the particle receiver, after absorbing thermal energy from the heliostat field's concentrated solar radiation. Meanwhile, h_z denotes the enthalpy of the sCO_2 at the outlet of the HEX-1 exchanger, which serves as the key variable for determining the temperature T_z.

$$\dot{m}_{DPS} C_{p,DPS} (T_{\text{Hot Particles}} - T_{\text{Cold Particles}}) = \epsilon_{HS} \dot{m} (h_z - h_x) \tag{35}$$

The heat exchangers HTR, LTR, and HEX-2 are governed by Eqs. (33) and (34), which defines the energy and mass balance between the hot and cold sides. In this equation, the heat exchanged on both sides of the heat exchanger is equated, incorporating its effectiveness into the analysis, denoted as ϵ_n. This effectiveness is assumed to be the same for all three exchangers. By applying this energy balance, the enthalpy values can be determined, allowing for the continuation of the cycle analysis.

In turbomachinery modeling, the process begins with the isentropic efficiency of the compressor η_{CP} and the gas turbine η_{GT}. These efficiencies make it possible to determine the actual power of both the compressor and the turbine, as well as the enthalpy at the outlet of each component. Eq. (36) presents the calculation of the actual power of the compressor. In an adiabatic process, the compression work corresponds to the enthalpy difference. Specifically, in a reversible adiabatic process, this difference matches the isentropic enthalpy change, as expressed in Eq. (37). To determine the temperature at the compressor outlet, Eq. (38) [30] is used. Since both the enthalpy and the pressure at state two are known, the temperature can be evaluated based on these parameters. For the power of the gas turbine the same process is performed as in the compressor, except that now there is an expansion. The Eq. (39) calculates the real power generated.

$$\dot{W}_{CP} = \frac{\dot{m} W_{is}}{\eta_{CP}} \tag{36}$$

$$W_{is} = h_{2s} - h_1 \tag{37}$$

Table 4
Properties of the fluids considered in the ORC [26,36,46,51].

Working fluid	T_c (K)	P_c (bar)	ODP	GWP/100 yr	Toxicity	Inflammability
R600	425.13	37.96	0	~20	A	A3
R600a	408.0	36.29	0	~20	A	A3
R1234yf	368.0	33.82	0	4	A	A2L
R1234ze(E)	382.0	36.35	0	6	A	A2L
R134a	374.0	40.59	0	1300	A	A1
R152a	386.0	45.17	0	124	A	A2
R114	419.04	32.4	1	10 000	A	A1
R245fa	472.0	36.51	0	1030	B	B1
Isopentane	460.4	33.7	0	~20	A	A3

$$\eta_{CP} = \frac{(\dot{W}_{CP}/\dot{m})_s}{(\dot{W}_{CP}/\dot{m})} = \frac{h_{2s} - h_1}{h_2 - h_1} \tag{38}$$

$$\dot{W}_{GT} = \dot{m}(h_3 - h_4) \tag{39}$$

The analysis inside the combustion chamber is made by using Eq. (40) [48] in which η_c is the combustion efficiency, $\dot{m}_f$ is the mass flow of the fuel and $\dot{Q}_{LHV}$ is the lower value of the heat combustion of the fuel. Thus, the total heat absorbed by the Brayton cycle is the sum of the contributions of the solar heat exchanger and the combustion of fuel ($\dot{Q}_h = \dot{Q}_{HS} + \dot{Q}_{HC}$). Finally, the waste heat, $\dot{Q}_L$, transferred to an organic Rankine cycle is evaluated from Eq. (41).

$$|\dot{Q}_{HC}| = \epsilon_{HC}\,|\dot{Q}_{z-3}| = \epsilon_{HC}\eta_c\dot{m}_f\dot{Q}_{LHV} \tag{40}$$

$$|\dot{Q}_L| = \dot{m}(h_{yx} - h_1) \tag{41}$$

The system performance is evaluated as shown in Eq. (42), where $\dot{W}_{Brayton,net}$ is the net power produced by the Brayton cycle, and is calculated in Eq. (43).

$$\eta_{Brayton} = \frac{\dot{W}_{Brayton,net}}{\dot{Q}_h} \tag{42}$$

$$\dot{W}_{Brayton,net} = \dot{W}_{GT} - \dot{W}_{CP} \tag{43}$$

2.3.2. Organic Rankine cycle (ORC)

The ORC is also evaluated by performing an energy balance on each component. The refrigerant used in the ORC is an important factor in the performance of the system. The refrigerants used must have near-zero Ozone Depletion Potential (ODP) and low Global Warming Potential (GWP). In this work, several refrigerants are considered in order to compare their performance. The choice of these refrigerants is based on environmentally friendliness, practically zero ODP, GWP lower than 150, low toxicity and low flammability [49,50]. The properties of the considered fluids are shown in Table 4.

The ORC cycle analysis is based on the input values presented in Table 3. The study begins with the energy balance in the HEX-2 heat exchanger, between the sCO_2 side and the ORC working fluid. This analysis is modeled in the Eq. (44).

$$\dot{m}(h_{yx} - h_1) = \varepsilon_n\dot{m}_o(h_{1o} - h_{4o}) \tag{44}$$

The steam turbine is modeled similarly to the gas turbine, considering the isentropic efficiency of the steam turbine, η_{VT} and the temperature T_{1_o} = 360K. The equation that describes this process is the Eq. (45). The temperature T_{2_o} is evaluated by knowing the actual enthalpy at the steam turbine outlet and the pressure P_{2_o}.

$$\dot{W}_{VT} = \dot{m}_o(h_{1_o} - h_{2_o}) \tag{45}$$

For the condenser, it is assumed that the fluid at the outlet is in a saturated liquid state. The thermal capacity of the condenser is determined by the Eq. (46), where the enthalpy h_{3_o} is calculated at the pressure P_{2_o} but with the quality corresponding to the outlet of the condenser. Finally, the pump power is obtained using the Eq. (47).

$$\dot{Q}_{cond} = \dot{m}_o(h_{2_o} - h_{3_o}) \tag{46}$$

$$\dot{W}_{pump} = \dot{m}_o(h_{4_o} - h_{3_o}) \tag{47}$$

The cycle performance is calculated as shown in Eq. (48), where $\dot{W}_{ORC,net}$ is the net power produced by the organic Rankine cycle, and is calculated as shown in Eq. (49).

$$\eta_{ORC} = \frac{\dot{W}_{ORC,net}}{\dot{Q}_L} \tag{48}$$

$$\dot{W}_{ORC,net} = \dot{W}_{VT} - \dot{W}_{pump} \tag{49}$$

2.4. Exergetic analysis

The exergy balance in each component of the SCBC/ORC power block and in the particle receivers is computed by performing the exergy analysis [30,52]:

$$\dot{W}_{cv} + \dot{E}_d = \sum \dot{E}_{qj} + \sum \dot{E}x_i - \sum \dot{E}x_e \tag{50}$$

$$\dot{E}x_i = \sum_{IN} \dot{m}e \tag{51}$$

$$\dot{E}x_e = \sum_{OUT} \dot{m}e \tag{52}$$

$$\dot{E}_{qj} = \left(1 - \frac{T_0}{T_j}\right)\dot{Q}_j \tag{53}$$

The exergy balance of each component is described in Appendix. $\dot{W}_{cv}$ is the rate work produced in the control volume, $\dot{E}_d$ is the rate of exergy destruction in each component. $\dot{E}_{qj}$ refers to the exergy rate of the heat transfer. $\dot{E}x_i$ is the input rate exergy to the control volume, and $\dot{E}x_e$ is the exit rate exergy to the control volume. In this work the magnetic, chemical, electrical, nuclear, kinetic and potential energy effects on the exergy analysis are not considered. The specific exergy can be calculated from the equation:

$$e = h - h_0 - T_0(s - s_0) \tag{54}$$

Where, h_0 is the dead state enthalpy and s_0 is the dead state entropy. To evaluate these dead states, T_0 = 298 K and P_0 = 1.013 bar are used.

The exergy efficiency of the combined cycle is defined by:

$$\eta_{ex} = \frac{\dot{W}_{net}}{\dot{E}_{in}} \tag{55}$$

Where $\dot{W}_{net} = \dot{W}_{Brayton,net} + \dot{W}_{ORC,net}$, see Eqs. (43) and (49). $\dot{E}_{in}$ is the exergy input coming to the power block from the combustion chamber and the particle receiver:

$$\dot{E}_{in} = \psi\left(\frac{\dot{Q}_{HS}}{\eta_{threc}\eta_{field}}\right) + \dot{Q}_{HC}\left(1 - \frac{T_0}{T_{HC}}\right) \tag{56}$$

The solar contribution in Eq. (56) is evaluated following the methodology proposed by Padilla et al. [53], $\dot{Q}_{HS}$ is the heat transferred in the solar heat exchanger, η_{field} is the efficiency of the heliostat field, for which in the present work we consider a value of 0.6 [54], and T_{HC} is the temperature of the combustion chamber. Finally, ψ is

Table 5
Comparison of present work with respect to the literature.

Data	Present work	Reyes-Belmonte *et al.* [33]	Relative error (%)
Particle mass flow (kg s⁻1)	120	121.9	1.5
Number of tubes	394	396	0.5
Absorption area (m^2)	129	143	9.7

the dimensionless maximum useful work available from solar radiation, which can be calculated from Petela's equation [55].

$$\psi = 1 - \frac{4}{3}\frac{T_0}{T_s} + \frac{1}{3}\left(\frac{T_0}{T_s}\right)^4 \tag{57}$$

Where T_s is the temperature of the Sun considered as a black body (∼ 5800 K).

3. Validation of the model

3.1. Particle receiver

For the particle receiver validation, the geometrical and heat transfer data used in the present work are compared with those reported in the literature. In this sense, the work of Reyes-Belmonte et al. [33] was taken as a reference, using the data from the medium-sized particle receiver and performing the same geometrical analysis conducted by Gallo et al. [28]. Table 5 shows the relative deviations ranging from 0.5% to 9.7% for the geometric part. By contrast, the convective heat transfer coefficient obtained in this study (α_{DPS} = 425.7 W/m^2K) falls within the range reported in the literature for dense particle suspensions [7,56]. Notably, the correlation employed here aligns with those previously proposed but distinguishes itself by incorporating more interactions than in Reyes-Belmonte work. Rather than relying on a limited set of empirical parameters, it captures the coupled effects of gas–particle thermal exchange, interparticle conduction, and radiative heat transfer among particles. This approach enables a more robust and physically grounded estimation of the convective coefficient, reflecting the inherent complexity of heat transfer in dense particle flows. These results support the choice of the parameters used in the modeling of the particle receiver.

3.2. Power cycle

In order to implement the power cycle model, air was initially used as the working fluid, since the TRNSYS 18 software [57] does not support simulations with supercritical carbon dioxide. This validation stage was carried out by directly comparing the results obtained from the Mathematica-developed code with those generated by TRNSYS, using air as the common working fluid. The comparison, presented in Table 6, shows excellent agreement between both data sets, with relative errors below 5% for all evaluated temperatures. The highest discrepancy appears at temperature t_z, corresponding to the outlet of the heat exchanger connected to the solar receiver, which is expected due to the transient behavior in that section of the system.

Although this procedure does not constitute a strict software-to-software comparison for the final working fluid (sCO_2), the ability of the Mathematica model to accurately replicate the system behavior using air, provides strong evidence of the correct implementation of energy and mass balances, as well as the system's dynamic behavior. This type of validation has been previously addressed. For example, Santos et al. [58] validated their model using dry air as the working fluid, comparing the results with experimental data from the SOLUGAS project. Once the model's accuracy was confirmed, they proceeded to analyze the system's performance using different working fluids. Thus, the procedure used for the application of the model to using supercritical CO_2 becomes structurally and functionally validated.

Table 6
Comparison of model using air with respect simulation in TRNSYS.

	Data	Present work (Air)	TRNSYS	Relative error (%)
Input	$\dot{m}$ (kg/s)	17.9	17.9	–
	r_p	4.5	4.5	–
	ϵ_{HS}	0.78	0.78	–
	ϵ_n	0.775	0.775	
	η_c	0.98	0.98	–
	η_{GT}	0.885	0.885	–
	η_{CP}	0.815	0.815	–
	t_1(°C)	25	25	–
Output	t_2(°C)	193	198	2.5
	t_{2x}(°C)	316	320	1.2
	t_x(°C)	493	504	2.1
	t_y(°C)	374	366	2.1
	t_z(°C)	653	622	4.9
	t_{yx}(°C)	242	245	1.2
	t_4(°C)	680	647	4.8

In this work, after confirming the model's consistency with air, simulations were then performed using sCO_2 as the working fluid, with thermophysical properties obtained from the REFPROP database [35]. While a direct cross-validation for sCO_2 is not possible due to TRNSYS limitations, the consistency of the model when using air supports the reliability of the results obtained with sCO_2, allowing the predictions to be considered representative of the real behavior of the system under operational conditions with this fluid.

4. Results and discussion

This section is devoted to a comprehensive analysis of the heat transfer in the particle receiver, the coupling of the receiver to the Brayton cycle, the organic Rankine cycle, and the exergetic analysis of the cycle.

4.1. Parametric analysis of the particle receiver

A parametric analysis is performed once the iterative process described in Section 2.2 is completed and all necessary variables are known in order to fix a receiver output temperature of 650 °C. The variables fixed in this iterative process are the input variables listed in Table 2. Now, some of these input variables are modified to perform a parametric analysis by analyzing the resulting behavior of the output data. The input data to be modified includes the tube diameter, the volumetric fraction, the gas velocity and the thermal radiation of the heliostat field. The results of the parametric analysis of the particle receiver are presented in Fig. 5. The tube diameter and the volumetric fraction of the fluidized bed present important influence on the thermal efficiency of the receiver. As shown in Fig. 5(a), the diameter of the tubes and the volumetric fraction of the particles lead to an increase in the receiver's efficiency. The tube diameter influences the number of tubes and is related to the heat transfer area, as indicated by Eqs. (10) and (11). Thus, a larger tube diameter implies a decrease in the number of tubes determining as well that the heat transfer area decreases, and also leading to a lower heat loss, followed by an increase of the efficiency of the receiver. Meanwhile, a higher volumetric fraction improves the heat transfer inside the receiver, leading to an efficiency increase, although it must be careful with the values chosen for those variables as it will be shown below. It is remarkable that considering values of 0.6 and 0.065 m for the volumetric fraction and tube diameter, respectively, the efficiency of the receiver can rise to 75%. Fig. 5(b) shows the behavior of the absorption area and the volumetric fraction with respect to the velocity of the fluidized bed. As the gas velocity increases, the area decreases because the number of tubes is inversely proportional to the mass flow per unit area, which in turn is directly proportional to the gas velocity and the difference between the gas velocity and the minimum fluidization velocity, see Eq. (1). Therefore,

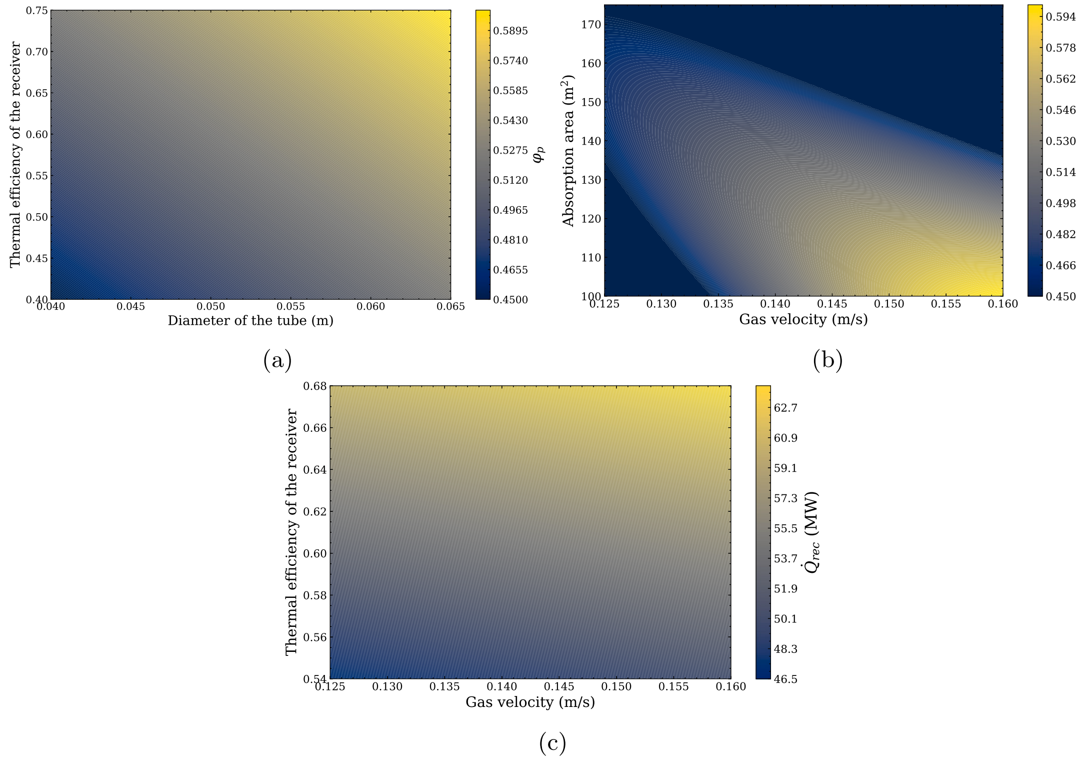

Fig. 5. Parametric analysis of particle receiver input variables. (a) Thermal efficiency of the receiver and variation of the volumetric fraction as a function of the diameter of the tube. (b) Absorption area and variation of the volumetric fraction as a function of the gas velocity. (c) Thermal efficiency of the receiver and variation of the thermal heat input of the heliostat field as a function of the gas velocity.

if the gas velocity is increased, the mass flow per unit area increases and the number of tubes decreases, which leads to a smaller heat transfer area.

In addition, an increase of the volumetric fraction leads to a smaller heat transfer area, which in turn is linked to the behavior observed in the previous graph, where increasing the volumetric fraction results in better heat transfer and a decrease of G_{DPS}. The latter determines that G_{DPS} has influence for both the geometrical part of the receiver and the heat transfer part. Fig. 5(c) shows that increasing gas velocity and thermal heat from the heliostat field improves the receiver's efficiency. It can be observed that an increase of the gas velocity up to 0.16 m/s and a thermal heat up to 65 MW lead to an increase of the receiver efficiency up to 68%. From Figs. 5(a) and 5(c) it can be noted that the tube diameter and volumetric fraction have a greater impact on the thermal efficiency than the gas velocity and thermal heat input. This is reflected in a 10.2% increase in the thermal efficiency of the receiver, which is obtained considering the highest values of the two graphs. In addition the effect of amount of heat coming from the heliostat field with respect to the temperature receiver can be analyzed. Although it has not been plotted in this work, this analysis requires that the temperature T_{fout} cannot be fixed and must be calculated from Eq. (7), determining a linear increase of T_{fout} with $\dot{Q}_{rec}$. Notice that, in this work, the fluidized bed temperature is equal to the particle outlet temperature ($T_{fout} = T_p^{out}$).

In Fig. 6(a) the behavior of the convective coefficient with respect to the gas velocity for different particle mass flows is presented. It shows that the convective coefficient is highly sensitive to the gas velocity. As the velocity increases from 0.125 m/s to 0.7 m/s, the convective coefficient increases by 142.35%. This behavior can be attributed to the dependence of the convection coefficient on dimensionless parameters, particularly the Reynolds number. The Reynolds number defines the flow regime, and when it surpasses 4000 ($Re \geq 4000$) [41], the flow transitions to turbulent, enhancing heat transfer by intensifying mixing mechanisms within the thermal boundary layer. In turbulent flow, eddies and fluctuations accelerate the transport of thermal energy between fluid layers, reducing thermal resistance and consequently increasing the convective heat transfer coefficient. In the context of heat transfer within a fluidized bed in the particle receiver, this relationship has been modeled using empirical and semi-empirical correlations (see Eqs. (12)–(21)). Specifically, Eq. (12) illustrates how α_{DPS} is influenced by both the wall convective coefficient (α_w) and the particle–tube radiative transfer (α_{rad}), underscoring the crucial role of turbulence in optimizing the system's thermal performance. In contrast, as it is also showed in Fig. 6(a), if the particle mass flow increases from 80 kg/s to 160 kg/s, the behavior of the convective coefficient does not change significantly, but if the particle mass flow rate is reduced, the convective coefficient increases. Thus, one might expect the system to perform better if $\dot{m}_p = 0$ when only airflow is present inside the receiver. However, as shown in Fig. 6(b), when the volumetric fraction of the suspension is reduced to 0.3, the receiver's thermal efficiency decreases to nearly zero. This is because the volumetric fraction is directly related to the mass flow per unit area, and as the volumetric fraction decreases, G_{DPS} is also reduced and the number of tubes rises, increasing the transfer area and heat loss by convection and radiation in the particle receiver. Hence, the particles inside the receiver act as effective heat transfer areas. If the mass flow rate of the particles decreases, this effective area influences the number of tubes and, consequently, the absorption area. In previous works [28] it is mentioned that the limiting volumetric fraction is a value of 0.63. In this work, the volumetric fraction of the suspension is 0.6.

4.2. Particle receiver interaction with the SCBC/ORC

Fig. 7 shows the interaction between the particle receiver and the Brayton cycle. In Fig. 7(a), shows the variation of the outlet temperature of the fluidized model and of the particle mass flow with respect to fuel mass flow. The fuel mass flow rate increases as the particle mass flow rate grows because the fluidized bed outlet temperature,

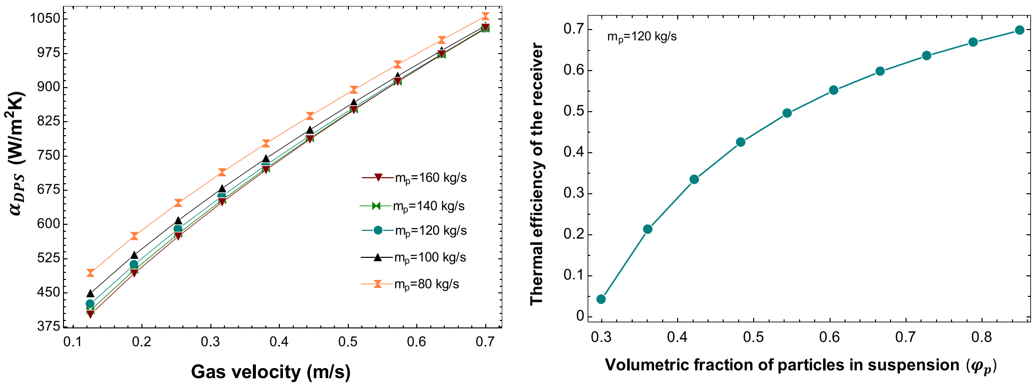

(a) (b)

Fig. 6. Parametric analysis of particle mass flow. (a) The convective coefficient at different mass flow rates of the particles a function of the gas velocity. (b) The thermal efficiency of the receiver with respect to the volumetric fraction of the suspension.

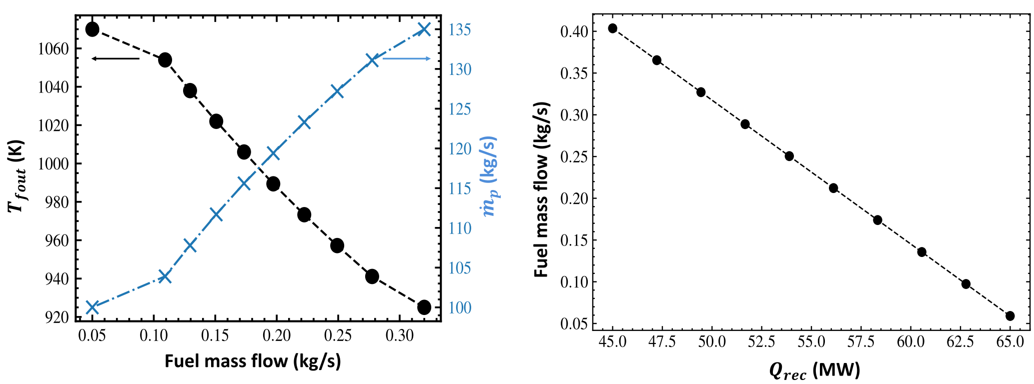

(a) (b)

Fig. 7. Interaction of the particle receiver with the Brayton cycle. (a) Variation of the outlet temperature of the fluidized model and of the particle mass flow with respect to fuel mass flow. (b) The fuel mass flow with respect to the thermal power of the heliostat field.

T_{fout}, decreases. This occurs since T_{fout} is inversely proportional to the fluidized bed mass flow ($\dot{m}_{DPS}$), see Eq. (9). If the particle mass flow rate increases, $\dot{m}_{DPS}$ also increases, causing T_{fout} to decrease. This results in higher fuel consumption. Additionally, Fig. 7(a) illustrates the behavior of the fuel mass flow consumed in the combustion chamber with respect to variations in the outlet temperature of the fluidized bed. It is evident from Fig. 7(a) that T_{fout} depends on the particle mass flow rate: the lower T_{fout}, the higher the fuel mass flow consumption in the combustion chamber.

In Fig. 7(b) the behavior of the fuel mass flow consumed in the combustion chamber with respect to the heat power coming from the receiver is presented. In Figs. 7(a) and 7(b), fuel mass flow is not considered as a fixed parameter for the sCO_2 Brayton power cycle in order to show its variation with respect to the receiver characteristic parameters. It can be observed that there is a point in the thermal power where the fuel mass flow is zero: $\dot{Q}_{rec}$ = 68.4 MW. This implies that if the heliostat field can deliver this power to the particle receiver, it would not be necessary to consume any fuel mass flow for power generation.

4.3. Organic rankine fluid choice

This section discusses the choice of working fluid for the ORC cycle to harness the waste heat power of the sCO_2 power Brayton cycle. For this purpose the refrigerants proposed in Section 2.3.2 have been analyzed. The study has been performed using input data from Table 3. The behavior of the energy and the exergetic efficiency with respect the compression ratio of the Brayton cycle is showed in Figs. 8(a) and 8(b), respectively, for the refrigerants considered. They show that R600 and R600a exhibit the best performance, both energetically and exergetically. For a better visualization, the behavior of R600 refrigerant is not plotted in Figs. 8(a) and 8(b), because it practically coincides with the one of R600a. It should be noted that both total energy and exergy efficiencies refer to the whole sCO_2 Brayton/ORC power system. The compression ratio is defined as the ratio between the inlet and outlet pressures of the fluid at the compressor. Refer to Figs. 1(a) and 1(c), where the isobars defined by these pressures are plotted on a T-s diagram. As the compression ratio, r_p, increases, the efficiency of the Brayton cycle increases significantly, influencing the behavior of the global efficiencies η_{Global} and η_{ex}. By varying the compression ratio, the outlet pressure of the compressor changes, which in turn affects the temperature of the subsequent heat exchange processes. This also impacts the bottoming ORC cycle, highlighting the importance of selecting an appropriate ORC to improve the global efficiency.

In order to analyze the influence of each device in the global exergy efficiency, the exergy destruction in each device has been evaluated for a r_p=4.5. Fig. 9(a) presents the exergy destruction in the different devices of sCO_2 Brayton cycle. Similarly, Fig. 9(b) shows the exergy destruction in each component of the ORC cycle. It can be seen that refrigerant R134a has the lowest exergy destruction compared to the other refrigerants, but presents a high GWP, see Table 4. Both R134a and Isopentane show a lower exergy destruction than R600a and R600, but energetically have a very poor performance. Therefore, R600a and R600 are the two working fluids that exhibit both the best conditions

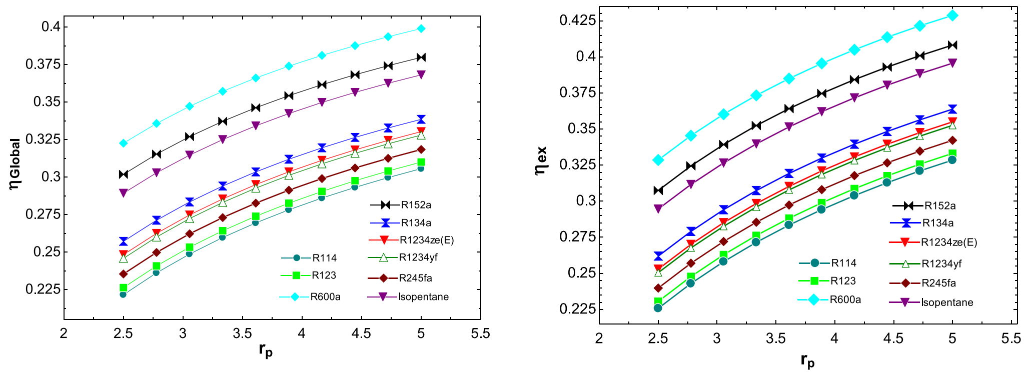

(a) (b)

Fig. 8. Analysis of the energy and exergy efficiency of different working fluids. (a) The overall energy efficiency with respect to the compression ratio of the cycle with different working fluids in the ORC is shown. (b) The overall exergy efficiency with respect to the variation of the compression ratio of the cycle with different working fluids in the ORC is shown.

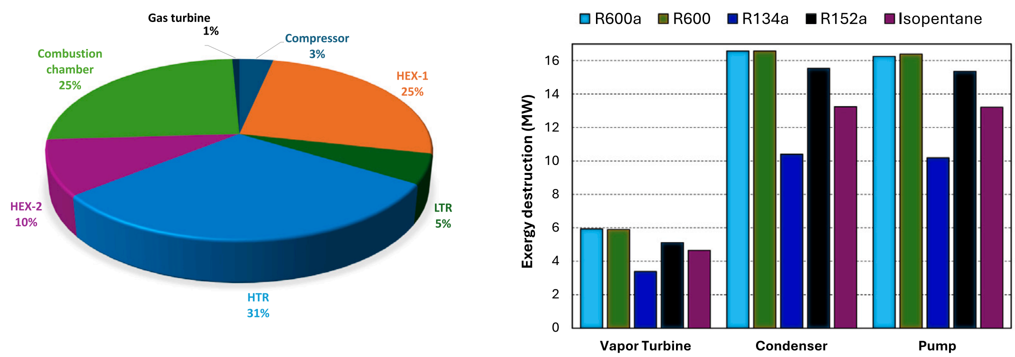

(a) (b)

Fig. 9. (a) Destruction of exergy in the Brayton cycle of supercritical CO_2. (b) Destruction of exergy in the organic Rankine cycle.

and good ODP and GWP values. R600a will be chosen for the study of the next section because it has lower exergy destruction in this study, and if we combine this with the global energy and exergy performance, it reveals as a good choice for analysis within the ORC.

The exergy destruction in each component is of particular interest because it indicates which component is more critical in terms of the energy quality loss. Fig. 9 shows the exergy destruction in each component of the SCBC/ORC system. The exergy destruction has a significant impact on the condenser and pump of the organic cycle, as shown in Fig. 9(b). The highest exergy destruction in the Brayton cycle was in the HTR with 31%, followed by HEX-1 and the combustion chamber with 25% each. The gas turbine and compressor show very low exergy destruction compared to the other components, as shown in Fig. 9(a). Although the organic fluids R600a and R600 have the same energetic and exergetic efficiencies, the exergy destruction in the pump has a higher value with R600, which is better appreciated in Fig. 9(b). It can be seen that the components with the highest exergy destruction are the heat exchangers, HEX-1 and HTR, and the condenser. This is caused by their temperatures, which are associated with high entropies and therefore with significant irreversibilities. In Fig. 9(b) it can be observed that R600 has the highest total exergy destruction in the pump. On the other hand, R134a has the lowest total exergy destruction, which for the condenser is a 37% smaller with respect to the obtained for the R600a, whereas its energy and exergy efficiency are only a 18.75% lower than the provided by R600a. Thus, R134a can be a good option for use in an ORC from an energetic and exergetic perspective. However, from an environmental standpoint, its GWP is significantly higher compared to R600a and R600.

4.4. Energy performance of SCBC/ORC

Then R600a is considered as the best choice based on both global energy and exergy criteria and from an environmental point of view. The presented results are specific for the choice of R600a as ORC working fluid, considering a particle volumetric fraction of the suspension of 0.6 and using the input data from Table 3. Now the fuel mass flow, the power produced, as well as the energy efficiency of each cycle are chosen as performance indicators. The results obtained for the energy performance are shown in Table 7. The net power includes the net power generated by the Brayton cycle plus ORC and is equal to 8.03 MW.

Under these conditions, the fuel consumption of the system was 0.196 kg/s. The fuel mass flow in the combustor chamber would increase to 0.32 kg/s if the solar input disappears, this represents a 63.2% increase in the fuel mass flow.

The working fluid used in the ORC is of great importance, as 36.9% of the total power generated by the SCBC/ORC cycle depends on it, as shown in Table 7. Fig. 10 illustrates the overall efficiency and total power as functions of the Brayton cycle input parameters and various ORC input temperatures of the vapor turbine. The compression ratio (r_p) varies between 2.5 and 5, while the ORC cycle inlet temperature (T_{1o}) ranges from 340 to 370 K, with both parameters changing simultaneously to assess their influence on the overall system efficiency. As illustrated in Fig. 10(a), the cycle's total energy efficiency can reach up to 40% when $r_p = 5$ and $T_{1o} = 370$ K. Adjusting T_{1o} directly affects the amount of heat recovered in the HEX-2 heat exchanger, thereby influencing its inlet temperature and ultimately impacting the

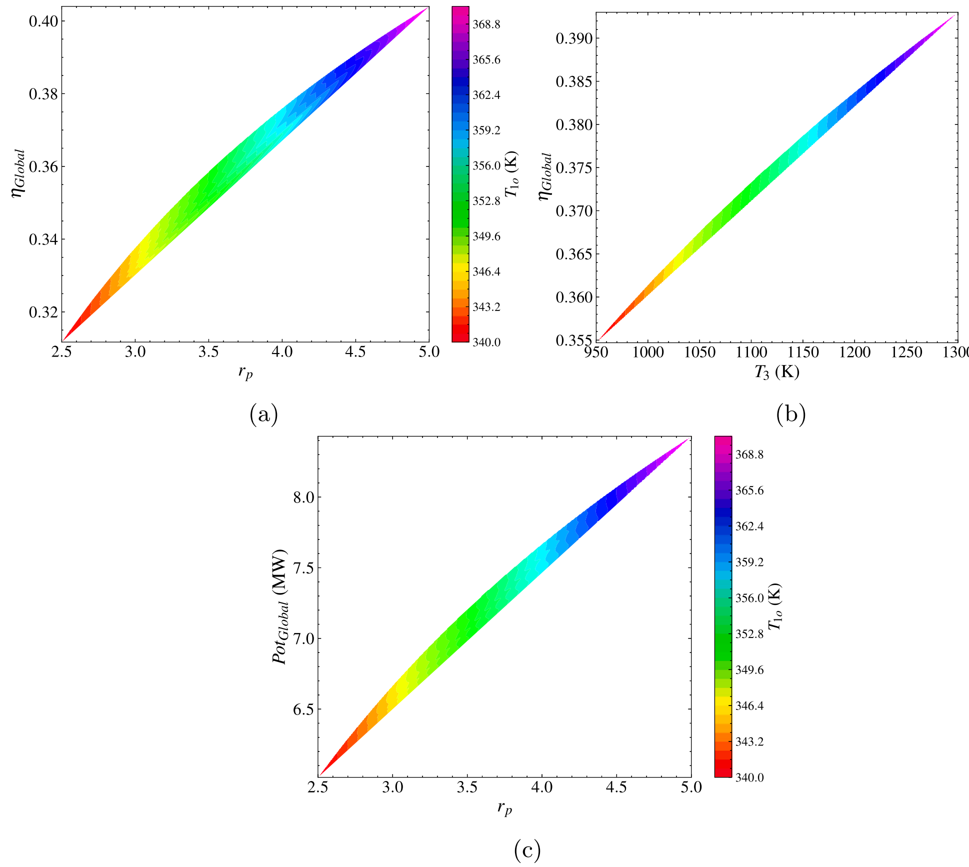

Fig. 10. Energy performance of SCBC/ORC cycle with respect to different vapor and gas turbine inlet temperatures and different compression ratios. (a) The global energy efficiency as a function of pressure ratio and vapor turbine inlet temperature (T_{1_o}). (b) The global power as a function of the inlet temperature to the steam turbine (T_{1_o}) and pressure ratio.

Table 7
Values obtained from the SCBC/ORC cycle analysis at the design point.

Component	Value
$\dot{W}_{GT}$ (MW)	5.54
$\dot{W}_{VT}$ (MW)	2.97
$\dot{W}_{CP}$ (MW)	0.46
$\dot{W}_{pump}$ (MW)	0.025
$\dot{m}_f$ (kg/s)	0.196
$\dot{Q}_L$ (MW)	6.2
$\dot{Q}_{HC}$ (MW)	5.4
$\dot{Q}_{HS}$ (MW)	7.0
η_{threc} (%)	58.4
$\eta_{Brayton}$(%)	35.3
η_{ORC}(%)	47.01
η_{Global}(%)	38.8
η_{ex}(%)	41.52

system's power output. This enhances the specific work output of the ORC cycle, contributing to an improvement in both energy and exergy efficiency. In Fig. 10(b), the maximum global energy efficiency that can be achieved is 39.0%, with input temperatures at the sCO_2 Brayton at ORC turbines T_3 = 1300 K and T_{1_o} = 370 K. In Fig. 10(c) the compression ratio is varied and a maximum power of 8.4 MW is obtained at T_{1_o} = 370 K and r_p = 5. The energy behavior of the system showed good performance in terms of both power output and energy efficiency.

4.5. Exergy analysis of the SCBC/ORC

The exergetic analysis of the system helps to determine the energy quality of the system, as well as the destruction of exergy in each component, which informs where an improvement can be made to achieve better performance. Fig. 11 shows the variation in the exergetic efficiency with the input parameters of the Brayton cycle, analyzing its behavior for different inlet temperatures of the ORC turbine. In Fig. 11(a) the highest exergetic efficiency has a value of η_{ex} = 0.435 and is obtained with a parameter combination of T_{1_o} = 370 K and r_p = 5. However, the system has the lowest exergetic quality when T_{1_o} = 340 K and r_p = 2.5. In Fig. 11(b) the inlet temperature of the sCO_2 Brayton turbine is varied, and the exergetic efficiency increases linearly with the temperature.

5. Conclusions

An energy and exergy analysis of a sCO_2 Brayton cycle integrated with an organic Rankine cycle coupled to a central tower solar receiver has been performed. It includes a detailed analysis of the heat transfer processes in the solar receiver for which a parametric analysis have been performed. The power block consisting on SCBC/ORC present remarkable results for both energy efficiency and net power output. For the ORC, several refrigerants have been analyzed, with R600a showing the best performance for the global SCBC/ORC. The exergy analysis performed for the system determines which components are associated with the highest irreversibilities. The main outcomes obtained are summarized as follows:

- **Analysis of the heat transfer of the particle receiver**: This analysis consider all the factors involved in this thermal energy transfer process. Semi-empirical correlations were used to model this process, which provide a good performance and good prediction of heat transfer. The convective coefficient was greater than 400 W/m^{2}K.

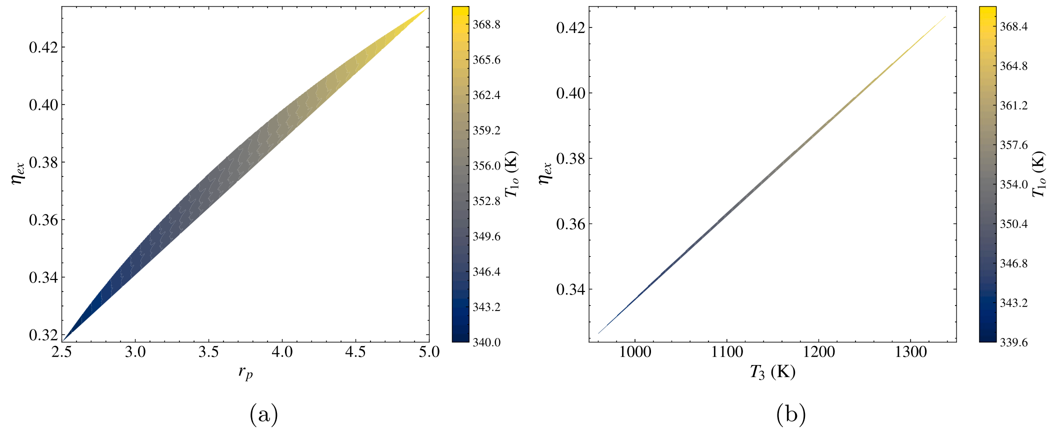

Fig. 11. Exergy analysis of the system with different inlet temperatures of the ORC turbine. (a) Exergetic efficiency with respect to compression ratio and the vapor turbine inlet temperature (T_{1_o}). (b) Exergetic efficiency with respect to the gas turbine inlet temperature (T_3) and the vapor turbine inlet temperature (T_{1_o}).

- **Particle receiver parametric analysis**: It considered the following variables: receiver outlet temperature, gas velocity, heliostat field heat input, tube diameter, convective coefficient, receiver thermal efficiency, and particle volumetric fraction. The latter is shown to be critical to achieve good thermal efficiency of the particle receiver, demonstrating the importance of maintaining a balance between particle mass flow rate, convective coefficient, and receiver thermal efficiency.
- **sCO_2/ORC**: The integration of a sCO_2 Brayton cycle with an Organic Rankine Cycle using a particle receiver significantly improves the overall efficiency. Since energy is wasted at the output of the sCO_2 turbine, an ORC is coupled to the sCO_2 to harness this thermal power potential. This scheme increases a 36.9% the energy production.
- **Fuel Consumption Reduction**: The study showed that the use of solar energy, specifically CSP, for power generation in conventional systems can result in a 62.3% reduction in fuel consumption. Moreover, in order to achieve full solar production, the thermal heat input of the heliostat field must be 68.4 MW.
- **Exergy Analysis**: The largest exergy destruction in the sCO_2 cycle occurs in the HTR, followed by HEX-1. In the ORC, the largest exergy destruction occurs in the condenser for both refrigerants R600 and R600a. This results determine that future efforts should focus on optimizing these components to improve system efficiency.
- **Optimal Working Fluid**: Among the various working fluids tested for the ORC, R600a (isobutane) was found to be the most efficient. Although R134a has the lowest exergy destruction among the considered refrigerants, R600a is chosen because it has better thermal and exergy performance and a lower GWP. This results highlights the importance of the choice of an appropriate working fluid from both an environmental point of view and to maximize the performance of the integrated system.

The relevance or these findings suggest further research in order to explore the multi-objective optimization of both the particle receiver design and the sCO_2 Brayton cycle, as well as to investigate the long-term operational stability and cost-effectiveness of the integrated system.

CRediT authorship contribution statement

J.A. Moctezuma-Hernandez: Writing – original draft, Visualization, Validation, Software, Formal analysis. **R.P. Merchán:** Writing – review & editing, Supervision. **J.M.M. Roco:** Writing – review & editing, Writing – original draft, Supervision.

Declaration of competing interest

The authors declare that they have no known competing financial interests or personal relationships that could have appeared to influence the work reported in this paper.

Acknowledgments

J.A.Moctezuma-Hernandez acknowledges financial support from CONACYT-México CVU 1006749. The authors acknowledge Universidad de Salamanca and funding from Ministerio de Ciencia, Innovación *y* Universidades of Spain under grant PID2023-147201OB-I00.

Appendix. Exergetic analysis

This appendix shows the exergy balance in each component of the particle receptor system, SCBC and ORC. From Eq. (62) only the exergy balance is shown without substituting the values of the exergy flux. However, in this work, HEX-1 with the particle receptor is considered as a single element.

Compressor (CP):

$$\dot{E}x_d = \dot{E}x_1 - \dot{E}x_2 + \dot{W}_{CP} \tag{58}$$

$$\dot{E}x_d = \dot{m}[(h_2 - h1) - T_0(s_2 - s_1)] + \dot{W}_{CP} \tag{59}$$

HEX-2:

$$\dot{E}x_{yx} + \dot{E}x_{4_o} = \dot{E}x_1 + \dot{E}x_{1_o} + \dot{E}x_d \tag{60}$$

$$\dot{E}x_d = \dot{m}[(h_{yx} - h_1) - T_0(s_{yx} - s_1)] - \dot{m}_o[(h_{4_o} - h_{1_o}) - T_0(s_{4_o} - s_{1_o})] \tag{61}$$

LTR:

$$\dot{E}x_2 + \dot{E}x_y = \dot{E}x_{2x} + \dot{E}x_{yx} + \dot{E}x_d \tag{62}$$

HTR :

$$\dot{E}x_{2x} + \dot{E}x_4 = \dot{E}x_y + \dot{E}x_x + \dot{E}x_d \tag{63}$$

HEX-1:

$$\dot{E}x_x + \left(1 - \frac{T_0}{T_H}\right)\dot{Q}_{HS} = \dot{E}x_2 + \dot{E}x_d \tag{64}$$

Combustion Chamber:

$$\dot{E}x_z + \left(1 - \frac{T_0}{T_H}\right)\dot{Q}_{HC} = \dot{E}x_3 + \dot{E}x_d \tag{65}$$

Gas turbine (GT):

$$\dot{E}x_3 = \dot{E}x_4 + \dot{W}_{GT} + \dot{E}x_d \tag{66}$$

Vapor turbine (VT):

$$\dot{E}x_{1_o} = \dot{E}x_{2_o} + \dot{W}_{VT} + \dot{E}x_d \tag{67}$$

Condenser ORC:

$$\dot{E}x_{2_o} + \left(1 - \frac{T_0}{T_H}\right)\dot{Q}_{cond} = \dot{E}x_{3_o} + \dot{E}x_d \tag{68}$$

Pump:

$$\dot{E}x_{3_o} + \dot{W}_{pump} = \dot{E}x_{4_o} + \dot{E}x_d \tag{69}$$

References

[1] I.P. on Climate Change (IPCC), Climate Change 2022 – Impacts, Adaptation and Vulnerability: Working Group II Contribution to the Sixth Assessment Report of the Intergovernmental Panel on Climate Change, Cambridge University Press, 2023, http://dx.doi.org/10.1017/9781009325844.

[2] J. Tian, L. Yu, R. Xue, S. Zhuang, Y. Shan, Global low-carbon energy transition in the post-COVID-19 era, Appl. Energy 307 (2022) 118205.

[3] IEA, Net zero by 2050, 2021, URL https://www.iea.org/reports/net-zero-by-2050.

[4] A. Modi, F. Bühler, J.G. Andreasen, F. Haglind, A review of solar energy based heat and power generation systems, Renew. Sustain. Energy Rev. 67 (2017) 1047–1064.

[5] K.R. Kumar, N.K. Chaitanya, N.S. Kumar, Solar thermal energy technologies and its applications for process heating and power generation–a review, J. Clean. Prod. 282 (2021) 125296.

[6] H. Zhang, J. Baeyens, J. Degrève, G. Cacères, Concentrated solar power plants: Review and design methodology, Renew. Sustain. Energy Rev. 22 (2013) 466–481.

[7] G. Flamant, D. Gauthier, H. Benoit, J.-L. Sans, R. Garcia, B. Boissière, R. Ansart, M. Hemati, Dense suspension of solid particles as a new heat transfer fluid for concentrated solar thermal plants: On-sun proof of concept, Chem. Eng. Sci. 102 (2013) 567–576.

[8] H. Benoit, I.P. López, D. Gauthier, G. Flamant, Temperature influence on wall-to-particle suspension heat transfer in a solar tubular receiver, in: AIP Conference Proceedings, vol. 1734, AIP Publishing, 2016.

[9] M. Silva-Pérez, Solar power towers using supercritical CO2 and supercritical steam cycles, and decoupled combined cycles, in: Advances in Concentrating Solar Thermal Research and Technology, Elsevier, 2017, pp. 383–402.

[10] Z. Liu, Z. Liu, X. Cao, T. Luo, X. Yang, Advanced exergoeconomic evaluation on supercritical carbon dioxide recompression Brayton cycle, J. Clean. Prod. 256 (2020) 120537.

[11] S. Mahmoudi, A. Ghavimi, Thermoeconomic analysis and multi objective optimization of a molten carbonate fuel cell–supercritical carbon dioxide–organic Rankin cycle integrated power system using liquefied natural gas as heat sink, Appl. Therm. Eng. 107 (2016) 1219–1232.

[12] K. Jiang, Y. Kong, C. Xu, Z. Ge, X. Du, Experimental performance of gas-solid countercurrent fluidized bed particle solar receiver with high-density suspension, Appl. Therm. Eng. 213 (2022) 118661.

[13] I.P. Lopez, H. Benoit, D. Gauthier, J.-L. Sans, E. Guillot, G. Mazza, G. Flamant, On-sun operation of a 150 kwth pilot solar receiver using dense particle suspension as heat transfer fluid, Sol. Energy 137 (2016) 463–476.

[14] B. Boissiere, R. Ansart, D. Gauthier, G. Flamant, M. Hemati, Experimental hydrodynamic study of gas-particle dense suspension upward flow for application as new heat transfer and storage fluid, Can. J. Chem. Eng. 93 (2) (2015) 317–330.

[15] C.S. Turchi, Z. Ma, T.W. Neises, M.J. Wagner, Thermodynamic study of advanced supercritical carbon dioxide power cycles for concentrating solar power systems, J. Sol. Energy Eng. 135 (4) (2013) 041007.

[16] M.-H. Kim, J. Pettersen, C.W. Bullard, Fundamental process and system design issues in CO2 vapor compression systems, Prog. Energy Combust. Sci. 30 (2) (2004) 119–174.

[17] L. Chen, B.-L. Deng, X.-R. Zhang, Experimental study of trans-critical and supercritical CO2 natural circulation flow in a closed loop, Appl. Therm. Eng. 59 (1–2) (2013) 1–13.

[18] R. Singh, M.P. Kearney, C. Manzie, Extremum-seeking control of a supercritical carbon-dioxide closed Brayton cycle in a direct-heated solar thermal power plant, Energy 60 (2013) 380–387.

[19] V. Dostal, P. Hejzlar, M.J. Driscoll, High-performance supercritical carbon dioxide cycle for next-generation nuclear reactors, Nucl. Technol. 154 (3) (2006) 265–282.

[20] S. Khatoon, M.-H. Kim, Preliminary design and assessment of concentrated solar power plant using supercritical carbon dioxide Brayton cycles, Energy Convers. Manage. 252 (2022) 115066.

[21] S. Hou, S. Cao, L. Yu, Y. Zhou, Y. Wu, F. Zhang, Performance optimization of combined supercritical CO2 recompression cycle and regenerative organic Rankine cycle using zeotropic mixture fluid, Energy Convers. Manage. 166 (2018) 187–200.

[22] H. Nami, S. Mahmoudi, A. Nemati, Exergy, economic and environmental impact assessment and optimization of a novel cogeneration system including a gas turbine, a supercritical CO2 and an organic Rankine cycle (GT-HRSG/SCO2), Appl. Therm. Eng. 110 (2017) 1315–1330.

[23] C. Wu, S.-s. Wang, J. Li, Exergoeconomic analysis and optimization of a combined supercritical carbon dioxide recompression Brayton/organic flash cycle for nuclear power plants, Energy Convers. Manage. 171 (2018) 936–952.

[24] X. Wang, Y. Yang, Y. Zheng, Y. Dai, Exergy and exergoeconomic analyses of a supercritical CO2 cycle for a cogeneration application, Energy 119 (2017) 971–982.

[25] M. Astolfi, D. Alfani, S. Lasala, E. Macchi, Comparison between ORC and CO2 power systems for the exploitation of low-medium temperature heat sources, Energy 161 (2018) 1250–1261.

[26] A.D. Akbari, S.M. Mahmoudi, Thermoeconomic analysis & optimization of the combined supercritical CO2 (carbon dioxide) recompression Brayton/organic Rankine cycle, Energy 78 (2014) 501–512.

[27] J. Tang, Q. Li, S. Wang, H. Yu, Thermo-economic optimization and comparative analysis of different organic flash cycles for the supercritical CO2 recompression Brayton cycle waste heat recovery, Energy 278 (2023) 128002.

[28] A. Gallo, J. Spelling, M. Romero, J. González-Aguilar, Preliminary design and performance analysis of a multi-megawatt scale dense particle suspension receiver, Energy Procedia 69 (2015) 388–397, http://dx.doi.org/10.1016/j.egypro.2015.03.045.

[29] J. Córcoles, M. Díaz-Heras, M. Fernández-Torrijos, J. Almendros-Ibáñez, Flow and heat transfer analysis of a gas–particle fluidized dense suspension in a tube for CSP applications, Renew. Energy 206 (2023) 1–12, http://dx.doi.org/10.1016/j.renene.2023.02.004.

[30] M.J. Moran, H.N. Shapiro, D.D. Boettner, M.B. Bailey, Fundamentals of Engineering Thermodynamics, John Wiley & Sons, 2010.

[31] I.W. Research, Mathematica, 2024, version 13.2, https://www.wolfram.com/mathematica/.

[32] S.A. Klein, Engineering equation solver (EES) v10.64, 2019, http://fchartsoftware.com/ees/.

[33] M. Reyes-Belmonte, A. Sebastián, J. Spelling, M. Romero, J. González-Aguilar, Annual performance of subcritical Rankine cycle coupled to an innovative particle receiver solar power plant, Renew. Energy 130 (2019) 786–795, http://dx.doi.org/10.1016/j.renene.2018.06.109.

[34] A.S. Cherkasova, Thermal Conductivity Enhancement in Micro- and Nano-Particle Suspensions, Rutgers The State University of New Jersey, School of Graduate Studies, 2009.

[35] E.W. Lemmon, M.L. Huber, M.O. McLinden, NIST standard reference database 23: Reference Fluid Thermodynamic and Transport Properties-REFPROP, Version 7.

[36] E. Lemmon, M. Huber, M. McLinden, NIST standard reference database 23, 2010, version 8.0, NIST, Gaithersburg.

[37] O. Molerus, K.-E. Wirth, Heat Transfer in Fluidized Beds, vol. 11, Springer Science & Business Media, 2012.

[38] W.-C. Yang, Handbook of Fluidization and Fluid-Particle Systems, CRC Press, 2003.

[39] M. Leva, M. Grummer, A correlation of solids turnovers in fluidized systems, Chem. Eng. Prog. 48 (6) (1952) 307–313.

[40] R. Turton, T. Fitzgerald, O. Levenspiel, An experimental method to determine the heat transfer coefficient between fine fluidized particles and air via changes in magnetic properties, Int. J. Heat Mass Transfer 32 (2) (1989) 289–296, http://dx.doi.org/10.1016/0017-9310(89)90176-2.

[41] T.L. Bergman, A.S. Lavine, F.P. Incropera, D.P. DeWitt, Introduction to Heat Transfer, John Wiley & Sons, 2011.

[42] E. Collings, F. Jelinek, J. Ho, M. Mathur, Magnetic and thermal properties of stainless steel and inconel at cryogenic temperatures, in: Advances in Cryogenic Engineering, vol. 22, Springer, 1977, pp. 159–173.

[43] J. Spelling, A. Gallo, M. Romero, J. González-Aguilar, A high-efficiency solar thermal power plant using a dense particle suspension as the heat transfer fluid, Energy Procedia 69 (2015) 1160–1170.

[44] M. Santos, R. Merchán, A. Medina, A.C. Hernández, Seasonal thermodynamic prediction of the performance of a hybrid solar gas-turbine power plant, Energy Convers. Manage. 115 (2016) 89–102.

[45] R. Korzynietz, D. Quero, R. Uhlig, et al., Solugus-Future Solar Hybrid Technology, Referiert, 2012.

[46] J.J. García-Pabón, D. Méndez-Méndez, J.M. Belman-Flores, J.M. Barroso-Maldonado, A. Khosravi, A review of recent research on the use of R1234yf as an environmentally friendly fluid in the organic Rankine cycle, Sustainability 13 (11) (2021) 5864.

[47] M. Yari, M. Sirousazar, A novel recompression S-CO_2 Brayton cycle with pre-cooler exergy utilization, Proc. Inst. Mech. Eng. Part A: J. Power Energy 224 (7) (2010) 931–946, http://dx.doi.org/10.1243/09576509JPE956.

[48] D. Olivenza-León, A. Medina, A.C. Hernández, Thermodynamic modeling of a hybrid solar gas-turbine power plant, Energy Convers. Manage. 93 (2015) 435–447, http://dx.doi.org/10.1016/j.enconman.2015.01.027.
[49] C. Wu, S.-s. Wang, J. Li, Exergoeconomic analysis and optimization of a combined supercritical carbon dioxide recompression Brayton/organic flash cycle for nuclear power plants, Energy Convers. Manage. 171 (2018) 936–952.
[50] P. Giménez-Prades, J. Navarro-Esbrí, C. Arpagaus, A. Fernández-Moreno, A. Mota-Babiloni, Novel molecules as working fluids for refrigeration, heat pump and organic Rankine cycle systems, Renew. Sustain. Energy Rev. 167 (2022) 112549.
[51] M. Grljušić, V. Medica, N. Račić, Thermodynamic analysis of a ship power plant operating with waste heat recovery through combined heat and power production, Energies 7 (11) (2014) 7368–7394.
[52] I. Dincer, M.A. Rosen, Exergy: Energy, Environment and Sustainable Development, Newnes, 2012.
[53] R.V. Padilla, Y.C.S. Too, R. Benito, W. Stein, Exergetic analysis of supercritical CO2 Brayton cycles integrated with solar central receivers, Appl. Energy 148 (2015) 348–365.
[54] C.K. Ho, B.D. Iverson, Review of high-temperature central receiver designs for concentrating solar power, Renew. Sustain. Energy Rev. 29 (2014) 835–846.
[55] R. Boehm, Maximum performance of solar heat engines, Appl. Energy 23 (4) (1986) 281–296.
[56] H. Zhang, H. Benoit, D. Gauthier, J. Degrève, J. Baeyens, I.P. López, M. Hemati, G. Flamant, Particle Circulation Loops in Solar Energy Capture and Storage: Gas–Solid Flow and Heat Transfer Considerations, Applied Energy 161 (2016) 206–224.
[57] S.A. Klein, TRNSYS, 2018, http://www.trnsys.com/.
[58] M.J. Santos, C. Miguel-Barbero, R.P. Merchán, A. Medina, A. Calvo Hernández, Roads to improve the performance of hybrid thermosolar gas turbine power plants: Working fluids and multi-stage configurations, Energy Convers. Manage. 165 (2018) 578–592.